Materials Advances

ROYAL SOCIETY OF CHEMISTRY

PAPER

View Article Online
View Journal | View Issue

Check for updates

Cite this: *Mater. Adv.*, 2025, **6**, 1971

Insights into the anticancer and anti-inflammatory activities of curcumin-loaded quercetin nanoparticles: *in vitro* bioassays coupled with synchrotron infrared microspectroscopy†

Suhair Sunoqrot, *[a] Samah Abusulieh[a] and Lina A. Dahabiyeh[b]

Curcumin (CUR) is an important phytochemical with diverse pharmacological activities, particularly in cancer treatment and inflammation management. However, its poor water solubility and rapid metabolism *in vivo* have limited its therapeutic potential, inspiring the development of delivery systems such as those based on nanotechnology. Previously, we reported that partial oxidation of the plant polyphenol quercetin (QCT) creates an amphiphilic material that self-assembles into discrete nanoparticles (NPs), either alone or with other polymers. Here we developed a nanoparticle (NP) formulation for CUR based on partially oxidized QCT (oxQCT). The NPs were co-formulated with D-α-tocopheryl poly(ethylene glycol) 1000 succinate (TPGS) to enhance their physicochemical properties and potentially synergize with CUR in inducing cancer cell death and alleviating inflammation. CUR was entrapped in oxQCT/TPGS NPs *via* nanoprecipitation, yielding spherical NPs (87 nm) with 72% loading efficiency, high colloidal stability, and sustained release at physiological pH. The anticancer activity of CUR NPs was evaluated in MCF-7 cells as a model breast cancer cell line, where the oxQCT/TPGS vehicle synergized with free CUR in inducing cell death and promoted its cellular uptake. In RAW 264.7 macrophages, the NPs outperformed free CUR in anti-inflammatory assays by exhibiting stronger reactive oxygen species (ROS) scavenging activities and attenuating the expression of proinflammatory cytokines. We complemented the biological assays with synchrotron-Fourier transform infrared microspectroscopy (SR-μFTIR), which provided insights into biochemical changes in the lipid and protein compositions of MCF-7 and RAW 264.7 macrophages treated with CUR NPs. Our findings present a promising nanoformulation for CUR which can enhance its activity against cancer and inflammation, and highlight the importance of bioanalytical techniques such as SR-μFTIR in discerning the bioactivities of multimodal nanotherapeutics.

Received 6th December 2024,
Accepted 12th February 2025

DOI: 10.1039/d4ma01202j

rsc.li/materials-advances

Open Access Article. Published on 14 February 2025. Downloaded on 4/6/2026 10:12:05 PM.
This article is licensed under a Creative Commons Attribution-NonCommercial 3.0 Unported Licence.

Introduction

Turmeric (*Curcuma longa* L.) has been used throughout history for medicinal purposes in Chinese medicine and Ayurveda.[1] Curcumin (CUR) is the principal component of turmeric rhizome and is commonly used for culinary and food coloring purposes. Previous studies have demonstrated the wide range of health benefits for CUR including antioxidant, anti-inflammatory, immunoregulatory, hepatoprotective, neuroprotective, antidiabetic, and anticancer properties.[2] In the context of cancer therapy, CUR is considered both as a preventative and as a therapeutic agent with minimal side effects compared to conventional chemotherapy. CUR exerts anticancer effects by interfering with oncogenic transcription factors, growth factors, inflammatory cytokines, and protein kinases involved in cancer progression.[3] Collectively, CUR can lead to the induction of cancer cell apoptosis and prevention of metastasis, invasion, as well as angiogenesis.[4] CUR's anti-inflammatory activity stems from its ability to modulate inflammatory signaling pathways and downregulate inflammatory mediators, including interleukins, tumor necrosis factor-α (TNF-α), and inducible nitric oxide synthase (iNOS).[5] These activities support the use of CUR for treating conditions such as rheumatoid arthritis, inflammatory bowel disease, and neurodegenerative diseases.[6]

Despite its numerous health benefits, CUR has low water solubility, poor bioavailability, and rapid metabolism *in vivo*, all of which hinder its clinical use.[7] Several formulation approaches have been investigated to improve the bioavailability and *in vivo* performance of CUR, particularly those based on

[a] *Department of Pharmacy, Faculty of Pharmacy, Al-Zaytoonah University of Jordan, Amman 11733, Jordan. E-mail: suhair.sunoqrot@zuj.edu.jo; Fax: +96264291432; Tel: +96264291511, ext. 471*
[b] *Department of Pharmaceutical Sciences, School of Pharmacy, The University of Jordan, Amman, Jordan*

† Electronic supplementary information (ESI) available. See DOI: https://doi.org/10.1039/d4ma01202j

© 2025 The Author(s). Published by the Royal Society of Chemistry

Open Access Article. Published on 14 February 2025. Downloaded on 4/6/2026 10:12:05 PM. This article is licensed under a Creative Commons Attribution-NonCommercial 3.0 Unported Licence.

colloidal delivery systems. Examples include micro- and nanoemulsions, liposomes, polymeric nanoparticles (NPs), and polymeric micelles.[8–11] Recently, plant polyphenols have gained significant interest as building blocks for functional materials including NP-based drug carriers.[12,13] NPs have been synthesized from plant polyphenols by relying on the propensity of these molecules to undergo oxidation-triggered coupling reactions and/or metal coordination.[14–16] Their polyphenolic structure enables them to form a variety of intermolecular interactions, including hydrogen bonding, π–π stacking, and van der Waals interactions, offering pharmaceutical scientists with green and easy-to-synthesize nanocarriers for the delivery of a wide range of drug molecules. The polyphenols which have been most extensively investigated in this regard are green tea catechins such as epigallocatechin gallate (EGCG),[17–19] tannic acid,[20] grape seed extracts,[21] and coffee bean extracts.[22]

Our group recently reported that the ubiquitous plant polyphenol quercetin (QCT) is capable of forming NPs upon oxidation in alkaline media, and the NPs could be used to load small drug molecules. The drug could be incorporated along with surface ligands during[23] or after NP formation.[24] We also showed that partial oxidation of QCT in an organic solvent such as dimethyl sulfoxide (DMSO) leads to the formation of supramolecular amphiphiles (oxQCT) which can later form NPs by self-assembly and co-assembly with hydrophilic and amphiphilic polymers *via* traditional nanoprecipitation.[25,26] oxQCT NPs represent a novel class of nanomaterials that have the potential to advance the development of nanomedicines for various biomedical applications including cancer and inflammation. However, there is still a gap in our fundamental understanding of the NPs' interactions with the bio-interface. A thorough understanding of the NPs' biological interactions with cancer cells and immune cells will be crucial in order to advance them further to pre-clinical and clinical testing. Advanced bioanalytical techniques such as synchrotron-Fourier transform infrared microspectroscopy (SR-μFTIR) can be of tremendous value in this aspect. This technique has emerged as a powerful non-invasive tool that can provide valuable chemical and spatial information on biomolecules within biological samples including blood, tissues, and individual cells, by probing the vibrational motions of their molecular constituents at a microscopic scale.[27] SR-μFTIR has been successfully used to identify biomolecular changes associated with cancer progression, cancer cell differentiation pathways, and the mechanisms of cancer cell death.[28] In terms of immunomodulation, μFTIR can provide important information about the biochemical changes occurring within immune cells in response to stimuli and treatment.[29] Having shown great potential as a drug delivery platform, the main aim of this study was to evaluate oxQCT as a nanocarrier for CUR. Following physicochemical characterization, the anticancer and anti-inflammatory activities of the NPs were evaluated in MCF-7 breast cancer cells and RAW 264.7 macrophages, respectively. In addition to conventional *in vitro* bioassays such as viability, uptake, apoptosis, and anti-inflammatory assays, we employed SR-μFTIR to provide additional insights into the diverse bioactivities of CUR and CUR-based nanocarriers.

Experimental section

Materials

Curcumin (CUR), quercetin hydrate (QCT), sodium metaperiodate ($NaIO_4$), D-α-tocopheryl poly(ethylene glycol) 1000 succinate (TPGS), 2,2-diphenyl-1-picrylhydrazyl (DPPH), and 3-(4,5-dimethylthiazol-2-yl)-2,5-diphenyltetrazolium bromide (MTT) were purchased from Sigma-Aldrich (USA). Lipopolysaccharide (LPS; *E. coli.* O55:B5) was obtained from ChemCruz (USA). JC-1 mitochondrial membrane potential dye was procured from Abcam (Cat No. ab141387, UK). Hydrogen peroxide (H_2O_2) was obtained from Scharlab (Spain). Potassium bromide (KBr) and dimethyl sulfoxide (DMSO) were purchased from Fisher Chemicals (UK). Spectra/Por dialysis membranes with 3.5 and 12–14 kDa molecular weight cut-offs (MWCO) were procured from Repligen (USA). Ultrapure water was prepared using an EMD Millipore Direct-Q 5UV system (USA). Phosphate buffered saline solution (PBS, 10×, pH 7.4) was purchased from EuroClone (Italy). Tween 80 was obtained from RCFL Limited (India).

Preparation of CUR-loaded oxQCT NPs

Amphiphilic partially oxidized QCT (oxQCT) was synthesized utilizing a 1 : 1 molar ratio of QCT : $NaIO_4$ as described in our earlier publications (Fig. 1(A)).[25,30] Briefly, QCT (1 g; 3.3 mmol) and $NaIO_4$ (708 mg; 3.3 mmol) were reacted in 20 mL DMSO for 24 h at room temperature. The solution was then dialyzed for 5 days against deionized water using a 3.5 kDa MWCO membrane, after which the purified material was lyophilized to obtain oxQCT powder which was used for NP preparation. CUR was loaded into TPGS-modified oxQCT NPs *via* nanoprecipitation, which involves the gradual addition of polymers and drug molecules dissolved in a water-miscible organic solvent to an aqueous phase under stirring, resulting in the formation of colloidal assemblies.[25] Briefly, stock solutions of CUR, TPGS, and oxQCT were prepared at 20 mg mL^{-1} in DMSO. Then, different amounts of CUR (0.5, 1, and 2 mg) were drawn from the stock solution and mixed with 5 mg of TPGS (250 μL) and 5 mg of oxQCT (250 μL) in a microtube. The organic phase was added dropwise to 2.5 mL of ultrapure water in a 10-mL glass vial protected from light under stirring at 500 rpm for 1 h to obtain a colloidal dispersion. The NPs were then dialyzed (3.5 kDa MWCO membrane) against deionized water for one day to remove the unentrapped drug with regular water changes, after which the NPs were collected and stored at 4 °C for further characterization. For the preparation of blank NPs (without CUR), the CUR solution was replaced with an equivalent volume of DMSO. A schematic representation of the preparation of CUR NPs is presented in Fig. 1(B).

Characterization of CUR-loaded oxQCT NPs

Evaluation of particle size and polydispersity. CUR-loaded NPs were characterized by measuring the particle size and polydispersity index (PDI) using dynamic light scattering (DLS). Samples were analyzed using a Nicomp Particle Sizing System (Nano Z3000, Entegris, USA). For the analysis, freshly prepared NPs were diluted 10 or 50 times with ultrapure water for size or zeta measurement, respectively. Results were reported as

© 2025 The Author(s). Published by the Royal Society of Chemistry

Open Access Article. Published on 14 February 2025. Downloaded on 4/6/2026 10:12:05 PM.
This article is licensed under a Creative Commons Attribution-NonCommercial 3.0 Unported Licence.

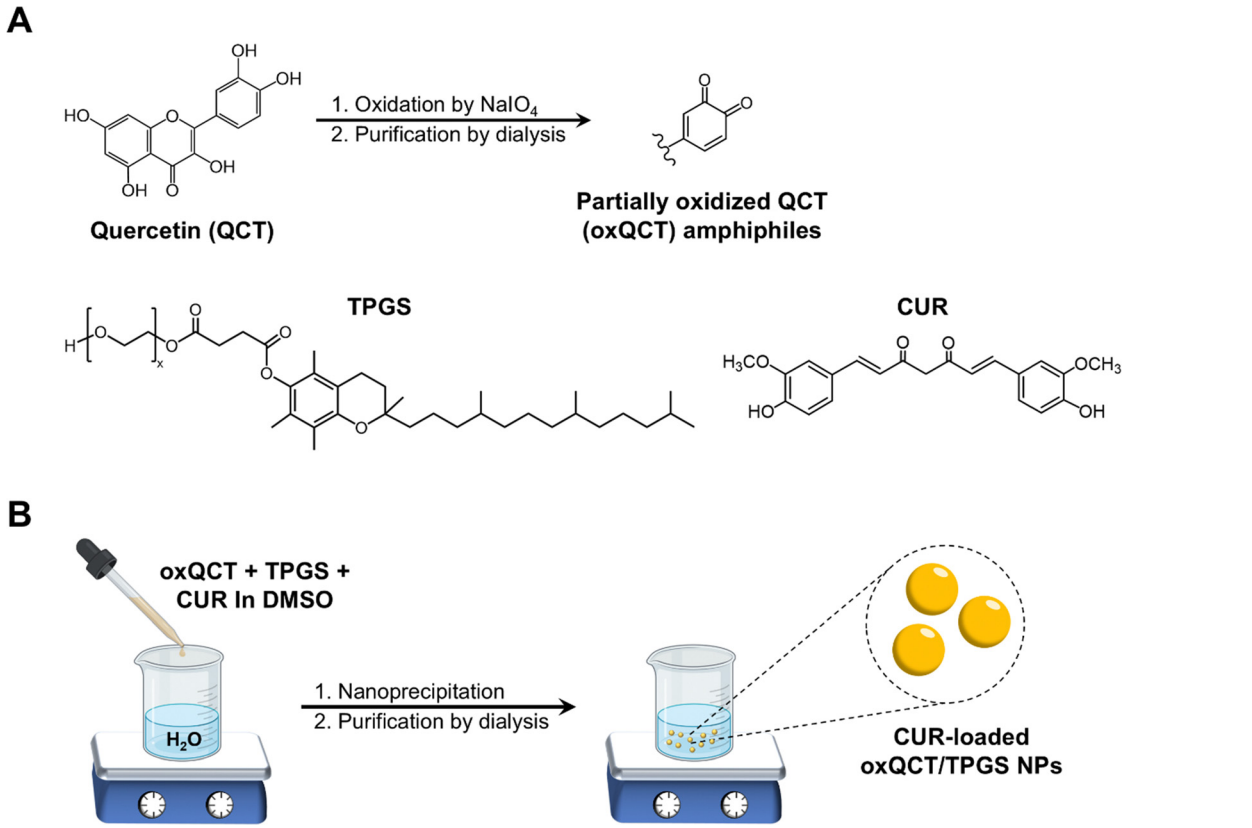

Fig. 1 (A) Structure of QCT and its oxidation by $NaIO_4$ to produce partially oxidized oxQCT amphiphiles; (B) preparation of CUR-loaded oxQCT/TPGS NPs by nanoprecipitation.

mean ± standard deviation (SD) from at least three different NP batches. For colloidal stability evaluation, triplicate samples of fresh CUR-loaded NPs were mixed 1 : 1 with PBS (pH 7.4), acetate buffer (pH 5.5), or complete Dulbecco's Modified Eagle's Medium (DMEM; EuroClone, Italy) supplemented with 10% fetal bovine serum (FBS; EuroClone). Samples were incubated at 37 °C for 1 h and then the particle size was measured by DLS as described above.

Drug loading efficiency (DL%) determination. The loading efficiency of CUR was determined by UV-Vis spectrophotometry (UV-1800, Shimadzu, Japan). Freshly prepared samples were diluted 50 times in DMSO and vortexed to break down the NPs, and the absorbance of CUR was measured at λ_{max} = 435 nm. A calibration curve of CUR absorbance *versus* concentration within the range of 5–0.3125 μg mL^{-1} in DMSO was constructed to calculate the concentration and amount loaded in the NPs. Data were representative of at least three different batches of NPs. Loading efficiency was calculated according to eqn (1):

$$\text{Drug loading efficiency (DL)\%} = \frac{\text{Actual amount of CUR loaded (mg)}}{\text{Initial amount of CUR added (mg)}} \times 100\% \quad (1)$$

***In vitro* release of CUR from loaded NPs.** The *in vitro* release of CUR from the NPs was evaluated at pH 7.4 and 37 °C to simulate physiologic conditions using the dialysis method. PBS (pH 7.4) with 0.5% w/v Tween 80 was used as the release medium to maintain sink conditions. One milliliter of fresh CUR NP dispersion was transferred to a dialysis bag (12–14 kDa MWCO) and tightly sealed. Then, the sample was immersed in 30 mL of the release medium in a 50-mL glass vial protected from light and incubated at 37 °C under shaking at 100 rpm in an orbital shaker-incubator (Biosan ES-20, Latvia). At predetermined time points (1, 2, 4, 6, 8 h), 10-mL samples were withdrawn from the vial and replaced with an equivalent volume of release medium. After 24, 48, 72, and 96 h, the entire medium was removed and replaced with 30 mL of fresh release medium. At the end of the experiment, CUR NPs remaining in the dialysis bags were collected and diluted 20 times in DMSO. The amount of CUR released from the NPs was measured by fluorescence spectroscopy as it offers a lower detection limit than UV-Vis. The fluorescence intensity of CUR in withdrawn samples was measured at 485 nm excitation and 528 nm emission wavelengths using a Synergy HTX Multi-Mode microplate reader (BioTek, USA). The fluorescence intensity of CUR in the remaining NPs (after dissolving in DMSO) was also measured to determine the amount remaining. The amount of CUR released or remaining was calculated based on a calibration curve of CUR fluorescence *versus* concentration (within the range of 5–0.3125 μg mL^{-1}) in the release medium or DMSO, respectively. Cumulative release (%) was calculated

Open Access Article. Published on 14 February 2025. Downloaded on 4/6/2026 10:12:05 PM. This article is licensed under a Creative Commons Attribution-NonCommercial 3.0 Unported Licence.

from the percentage ratio of the cumulative amount of released CUR at each time interval to the total amount of CUR in the NPs. The cumulative release (%) of CUR was plotted against time (h) to obtain the release profile. The experiment was performed in triplicate. To understand the mechanism of CUR release, the release data up to 60% cumulative release were fitted to the Korsmeyer–Peppas model (eqn (2)):[31]

$$Q_t = kt^n \quad (2)$$

where Q_t represents the cumulative % amount of the drug released at time t, k is the release rate constant, and n is the release exponent which is related to the mechanism of drug release from polymeric delivery systems.[32]

In vitro antiproliferative activity of CUR-loaded NPs

Cell culture conditions. The MCF-7 breast cancer cell line was obtained from the American Type Culture Collection (ATCC, USA). Cells were cultured in complete growth medium in T-75 cm^2 culture flasks and maintained in a humidified 5% CO_2 incubator at 37 °C. Complete growth medium consisted of Minimum Essential Medium (MEM; EuroClone, Italy) supplemented with 10% heat-inactivated fetal bovine serum (FBS; EuroClone) and 1% penicillin–streptomycin (100 U mL^{-1}–100 μg mL^{-1}; EuroClone). The medium was renewed and cells were sub-cultured using trypsin/EDTA solution (EuroClone) twice a week. To perform the experiments, cell culture flasks were used at passages between 5 and 10 and 80–90% confluency.

Cell viability assay. The antiproliferative activity of CUR NPs against MCF-7 cells was evaluated using an MTT assay. Briefly, cells were seeded in 96-well plates at a density of 10 000 cells per well and allowed to adhere overnight. The next day, cells (n = 5 per treatment group) were treated with different concentrations of CUR (300, 100, 10, 1, and 0.1 μM) in the form of free-CUR (from a 20 mg mL^{-1} stock solution in DMSO) and CUR-loaded NPs (freshly prepared aqueous dispersions) diluted in the complete medium for 24, 48, and 72 h. Cells were also treated with blank (CUR-free) NPs at concentrations equivalent to CUR-loaded NPs. At the end of each incubation period, the medium in each well was replaced with 100 μL of fresh medium containing 0.5 mg mL^{-1} MTT and cells were incubated for another 3 h in the CO_2 incubator. The supernatant was then carefully removed, and 100 μL of DMSO was added followed by further incubation in an orbital shaker incubator (100 rpm, 37 °C, 10 min) to ensure complete dissolution of formazan crystals. The absorbance intensity of each well which is proportional to the number of viable cells was measured at 540 nm using a Synergy HTX Multi-Mode microplate reader. Cell viability (%) was calculated from the percentage ratio of the absorbance of each treatment group relative to the untreated control group. The half maximal inhibitory concentration (IC_{50}) values were determined by non-linear regression analysis of cell viability *versus* concentration curves using GraphPad Prism software version 9 (USA). To evaluate potential synergism between CUR and the oxQCT/TPGS NP vehicle, the IC_{50} of free CUR and that of the empty NPs were used to calculate the combination index (CI) based on the Chou–Talalay method according to eqn (3):[33]

$$\text{Combination index (CI)} = \frac{D_1}{D_{x1}} + \frac{D_2}{D_{x2}} \quad (3)$$

where D_1 and D_2 are the IC_{50} values for CUR and the NP vehicle in CUR-loaded NPs after 72 h of incubation, respectively, and D_{x1} and D_{x2} are the IC_{50} values for free CUR and the empty NPs after 72 h of incubation, respectively.

JC-1 mitochondrial membrane potential assay. Depolarization of the mitochondrial membrane potential in MCF-7 cells after treatments with CUR NPs was evaluated using a JC-1 assay as previously described.[34] The assay utilizes the JC-1 probe that forms red fluorescent aggregates inside intact mitochondria, which are converted to green fluorescent monomers upon depolarization of the mitochondrial membrane as a sign of early apoptosis. Cells were seeded in a 96-well plate at 10 000 cells per well (n = 3), and treated with CUR, CUR NPs, or blank NPs at a concentration equivalent to 20 μM CUR diluted in complete culture medium. After 24 h of treatment, 100 μL of 20 μM JC-1 dye solution was added directly to each well and cells were stained for 10 min at 37 °C. The green fluorescence of JC-1 monomers was detected at 485 nm/528 nm, and the red fluorescence of JC-1 aggregates at 540/620 nm excitation/emission wavelengths using a Synergy HTX Multi-Mode microplate reader. The results were expressed as a ratio of JC-1 monomer/aggregate fluorescence normalized relative to the untreated cells.

Caspase activity assay. The activity of caspase-3 and caspase-8 in MCF-7 cells treated with CUR NPs was examined using a Caspase Multiplex Activity Assay kit (Abcam, Cat No. ab219915, UK) following the manufacturer's instructions. Cells were seeded in a 96-well plate at 10 000 cells per well (n = 3) overnight, and then treated with 20 μM of CUR, CUR NPs, or blank NPs diluted in complete medium. After 24 h of treatment, 100 μL of the caspase mix was added directly to each well and incubated for 1 h at 37 °C. The red fluorescence of caspase-3 and the green fluorescence of caspase-8 were measured at 540/620 nm and 485/528 nm excitation/emission wavelengths, respectively, using a Synergy HTX Multi-Mode microplate reader. Results were expressed as the mean fold increase in fluorescence intensity of treated cells relative to untreated controls.

Anti-inflammatory activity of CUR-loaded NPs

DPPH antioxidant assay. DPPH radical scavenging capacity of CUR NPs compared to free CUR was assessed as a measure of antioxidant activity.[35] Briefly, CUR, CUR NPs, and blank NPs were diluted in DMSO to obtain different concentrations of CUR (3.125, 6.25, 12.5, 25, 50, and 100 μg mL^{-1}), then 0.2 mL of each dilution or DMSO (as the solvent blank) was mixed with 4 mL of DPPH solution (0.1 mM in ethanol). Solutions were incubated in the dark at room temperature for 30 min, then the absorbance was measured at 517 nm using a microplate reader. The experiment was performed in triplicate. The DPPH radical

© 2025 The Author(s). Published by the Royal Society of Chemistry

Open Access Article. Published on 14 February 2025. Downloaded on 4/6/2026 10:12:05 PM. This article is licensed under a Creative Commons Attribution-NonCommercial 3.0 Unported Licence.

scavenging activity (%) was calculated according to eqn (4):

$$\text{Scavenging activity (\%)} = \left(1 - \frac{\text{Absorbance of the sample}}{\text{Absorbance of the blank}}\right) \times 100\% \quad (4)$$

Measurement of intracellular reactive oxygen species (ROS) in H_2O_2-stimulated RAW 264.7 macrophages. The *in vitro* antioxidant activity of CUR-loaded NPs compared to free CUR was assessed by measuring their ability to suppress the production of reactive oxygen species (ROS) in H_2O_2-stimulated RAW 264.7 murine macrophages (obtained from ATCC). ROS detection was performed using a 2′,7′-dichlorodihydrofluorescein diacetate (DCFDA) Cellular ROS Detection Assay Kit (Abcam: ab113851, UK) as previously described with some modification.[36] For all experiments, cells were cultured in complete growth medium in T-75 cm^2 culture flasks and maintained in a humidified 5% CO_2 incubator at 37 °C. Complete growth medium consisted of DMEM (Euroclone) supplemented with 10% heat-inactivated FBS and 1% penicillin–streptomycin (100 U mL^{-1}–100 μg mL^{-1}). The culture medium was changed routinely and cells were detached from the culture flask using a cell scraper and subcultured in a new flask every 2 to 3 days. To perform the experiments, cells were used at passages between 4 and 8. When the cells reached 70–80% confluency, they were detached from the flask using a cell scraper, counted, and seeded at 10 000 cells per well in a 96-well plate overnight. The next day, cells (n = 3) were treated with 20 μM CUR, CUR NPs, and blank NPs diluted in complete medium. After 24 h of treatment, the medium in each well was replaced with 100 μL fresh medium containing 20 μM DCFDA and 350 μM H_2O_2 and the cells were incubated for 45 min at 37 °C. Another group of cells was treated with 100 μL fresh medium containing 20 μM DCFDA only (unstimulated cells). The experiment depends on the oxidation of the non-fluorescent DCFDA by cellular esterases in the presence of intracellular ROS to the highly fluorescent molecule 2′,7′-dichlorofluorescein (DCF). After 45 min of incubation, the medium in each well was replaced with fresh PBS and DCF fluorescence was read with a microplate reader at 485 nm/528 nm excitation/emission wavelengths. Results were expressed as the fold increase in DCF fluorescence relative to untreated and unstimulated cells.

Anti-inflammatory activity of CUR NPs in LPS-stimulated RAW 264.7 macrophages. The anti-inflammatory activity of CUR NPs was assessed in an LPS-stimulated RAW 264.7 macrophage model as previously described.[37] Cells were seeded at 10 000 cells per well in a 96-well plate overnight, and then co-treated (n = 3) with 100 μL of 1 μg mL^{-1} LPS and 20 μM CUR, CUR NPs, or blank NPs for 24 h at 37 °C. The control group received 100 μL of fresh medium (unstimulated and untreated cells). Another group of cells received 100 μL of 1 μg mL^{-1} LPS only (stimulated and untreated cells). The following day, the supernatant of each well (100 μL) was collected in a separate microtube and stored at −80 °C. The collected supernatants were analyzed to measure the levels of secreted proinflammatory cytokines (TNF-α, Il-1β, and IL-6) using TNF-α (Cat No. BMS622, Invitrogen, USA), Il-1β (BMS630, Invitrogen), and IL-6 (BMS625, Invitrogen) Enzyme-linked Immunosorbent Assay (ELISA) kits following the manufacturer's instructions. Cell supernatants were diluted with the sample diluent provided in the kits (2 times for IL-1β and IL-6 and 20 times for TNF-α) prior to the analyses. The concentration of each proinflammatory cytokine in each sample was then calculated based on its respective standard curve, and the results were expressed as the mean concentration of each cytokine ± SD for each treatment group.

Cellular uptake of CUR NPs by flow cytometry and fluorescence imaging

The quantitative uptake of CUR NPs by MCF-7 cells and RAW 264.7 macrophages compared to free CUR was carried out using flow cytometry by relying on the intrinsic green fluorescence of CUR. Cells were seeded in 24-well plates at a density of 50 000 cells per well (RAW 264.7) or 100 000 cells per well (MCF-7) in triplicate and incubated with their compatible culture media overnight. The next day, cells were incubated with 20 μM free CUR or CUR NPs in 0.5 mL of serum-free medium for 1 and 4 h. At the end of the incubation period, cells were washed gently with PBS, and detached in 0.1 mL per well PBS using a scraper (RAW 264.7) or incubated with 0.1 mL per well trypsin at 37 °C for 5–10 min (MCF-7). Then, the cells were collected with PBS, centrifuged at 150 × g for 5 min, and resuspended in 0.5 mL PBS. Cell-associated fluorescence was measured immediately using the green fluorescence channel (FL-1) of a BD Accuri C6 Plus Flow Cytometer (BD Biosciences, USA) with the threshold set to 10 000 events. Analysis was performed using BD Accuri C6 Plus software. The results were expressed as the fold increase in fluorescence count relative to untreated cells.

For visualization of cellular uptake by fluorescence imaging, cells were treated as described above for flow cytometry. At the end of the incubation period, cells were washed gently with PBS and fixed with 4% paraformaldehyde (0.2 mL per well) for 10 min. After washing with PBS, cells were imaged using a ZOE Fluorescent Cell Imager (Bio-Rad Laboratories, USA) using the green channel.

Synchrotron FTIR microspectroscopy (SR-μFTIR)

Cell treatment. MCF-7 and RAW 264.7 macrophages were each seeded at 75 000 cells per well on top of 13 mm × 1 mm CaF_2 IR transmission windows (Crystran Ltd, Poole, UK) which were placed at the bottom of 24-well plates in duplicate. After 24 h, cells were treated with free CUR, CUR NPs, or blank NPs at a concentration equivalent to 20 μM CUR. In the case of RAW 264.7 macrophages, cells were treated with LPS (1 μg mL^{-1}) alone or co-treated with LPS (1 μg mL^{-1}) + free CUR, CUR NPs, or blank NPs at a concentration equivalent to 20 μM CUR. All treatments lasted for 24 h. At the end of the incubation period, the media was carefully removed and the cells were fixed with 4% paraformaldehyde for 50 min at room temperature. After that, the slides were gently washed with PBS twice and left to dry at room temperature. The slides were then

Open Access Article. Published on 14 February 2025. Downloaded on 4/6/2026 10:12:05 PM.
This article is licensed under a Creative Commons Attribution-NonCommercial 3.0 Unported Licence.

transferred using forceps to dedicated sample holders until measurement.

SR-μFTIR measurements. SR-μFTIR data were acquired at the Synchrotron Light for Experimental Science and Applications in the Middle East (SESAME; Allan, Jordan) BM02-IR beamline.[38,39] The beamline end station comprises a Bruker Hyperion 3000 IR-Vis microscope (Bruker Optik GmbH, Ettingen, Germany) equipped with a mercury cadmium telluride (MCT) single point detector. The microscope is coupled to a Bruker Vertex 70v FTIR spectrometer. OPUS© v. 8.5. SP1 Bruker software package was used for data acquisition in the transmission mode on CaF_2 IR transmission windows with a pair of 15× Schwarzschild objective and condenser, and a beam aperture of 30 μm × 30 μm in the mid-IR region (4000–650 cm^{-1}), with 64 co-added scans at a spectral resolution of 4 cm^{-1}. Levels Zero filling 2, and Blackman–Harris 3-Term apodization window were used. Background spectra were measured prior to each sample to assess its spectral contribution.

Data treatment and statistical analysis. The collected raw spectra were processed using the multivariate statistical analysis software The Unscrambler X 10.4 (CAMO Analytics, Norway) as previously described.[40–43] Briefly, two absorption spectral regions were identified: lipid CH stretching (2800–3050 cm^{-1}) and protein (amide I and II)-carbonyl vibrations (1485–1855 cm^{-1}). Spectra were baseline-corrected and smoothed with 7 points window using the Savitzky–Golay smoothing algorithm. For normalization, spectra of the lipid region were unit vector normalized while the protein-carbonyl spectral region was first differentiated using Savitsky–Golay second derivatives and then range normalized. Principal component analysis (PCA) was performed on each of the two predefined spectral ranges and results were presented as score and loading plots. The normalized reduced average spectrum for each data set and the normalized reduced Savitsky–Golay second derivative average spectrum (for the protein-carbonyl region) were used to identify spectral differences between the different groups.

Results and discussion

Preparation and characterization of CUR-loaded oxQCT/TPGS NPs

We have previously shown that QCT can undergo oxidative coupling reactions in basic media[23,24] or in the presence of oxidizing agents such as $NaIO_4$,[30] leading to the formation of an amphiphilic material capable of self-assembly into NPs. The method is similar to the formation of NPs upon oxidation of green tea catechins.[44] We have also shown that partially oxidized QCT (oxQCT) can co-assemble with polymers such as poly(ethylene glycol), poloxamers, and TPGS during NP formation by nanoprecipitation. Moreover, co-assembling oxQCT with these polymers could modulate the NPs' cellular interactions by promoting apoptosis and synergizing with bioactive natural products.[25,26] Having shown promise as a drug delivery platform, we decided to explore oxQCT as a nanocarrier for CUR, focusing on CUR's prominent bioactivities in cancer and inflammation. The NPs were co-assembled with TPGS as this polymeric excipient possesses notable antioxidant and anticancer properties,[45] which could synergize with CUR and enhance its therapeutic action.

Table 1 Characterization of CUR-loaded and blank NPs co-assembled with TPGS (mean ± SD; n = 3)

Formulation	Particle size (nm)	PDI	Loading efficiency (%)
Blank NPs	60 ± 1	0.25 ± 0.02	—
CUR NPs_0.5	81 ± 10	0.15 ± 0.04	82 ± 1
CUR NPs_1	87 ± 4	0.14 ± 0.09	72 ± 1
CUR NPs_2	88 ± 8	0.16 ± 0.01	33 ± 1

As shown in Table 1, CUR-free NPs (blank NPs) exhibited a particle size of 60 nm and a PDI of 0.25. Upon CUR loading, an increase in particle size was noted at all loading levels, most likely due to drug entrapment within the NP matrix. All CUR-loaded NPs exhibited low PDI values ranging between 0.14 and 0.16. CUR-loaded NPs at 0.5 and 1 mg per batch achieved high loading efficiencies of 82 and 72%, respectively. Based on the structure of CUR, QCT, and TPGS (Fig. 1(A)), CUR was most likely entrapped within the NPs by hydrogen bonding, π–π stacking, and/or hydrophobic interactions, contributing to the excellent loading efficiency. However, increasing the CUR amount to 2 mg per batch (20% by weight of oxQCT/TPGS) significantly reduced the loading efficiency to 33%, which could indicate that the amount of CUR exceeded the capacity of the nanocarrier. Based on these results, the formulation CUR NPs_1 was chosen for further experiments as it contained the highest loaded amount of CUR compared to the other formulations.

As demonstrated in Fig. 2(A), the optimal CUR NPs were associated with a narrow particle size distribution and spherical morphology. The UV-Vis spectrum of CUR (Fig. 2(B)) showed the characteristic peak at λ_{max} = 430 nm, which remained unchanged after loading in CUR NPs, denoting that the nanoprecipitation process did not affect CUR's stability. The NP formulation also displayed excellent colloidal stability under different conditions, such as physiologic (7.4) and acidic pH (5.5), and in the presence of serum-supplemented cell culture media (Fig. 2(C)). As for drug release, a problem which could be encountered in colloidal systems is the burst release effect due to the high surface area-to-volume ratio at the nanoscale. As shown in Fig. 2(D), CUR NPs exhibited slow and sustained release at pH 7.4, with 35% cumulative release after 8 h, and 76–99% cumulative release between 24–96 h. Fitting the release data to the Korsmeyer–Peppas model resulted in a regression coefficient (R^2) of 0.995, indicating an excellent fit with the model. Moreover, the release exponent n, which is employed to explain the drug release mechanism, was found to be 1.6. Since this value is greater than 0.85, it is assumed that CUR release followed supercase II transport through a combination of polymer relaxation and swelling.[32] The ability of the NP vehicle to sustained CUR release will be valuable in *in vivo* applications, by protecting the drug from premature elimination while promoting its tissue uptake.

© 2025 The Author(s). Published by the Royal Society of Chemistry

Open Access Article. Published on 14 February 2025. Downloaded on 4/6/2026 10:12:05 PM.
This article is licensed under a Creative Commons Attribution-NonCommercial 3.0 Unported Licence.

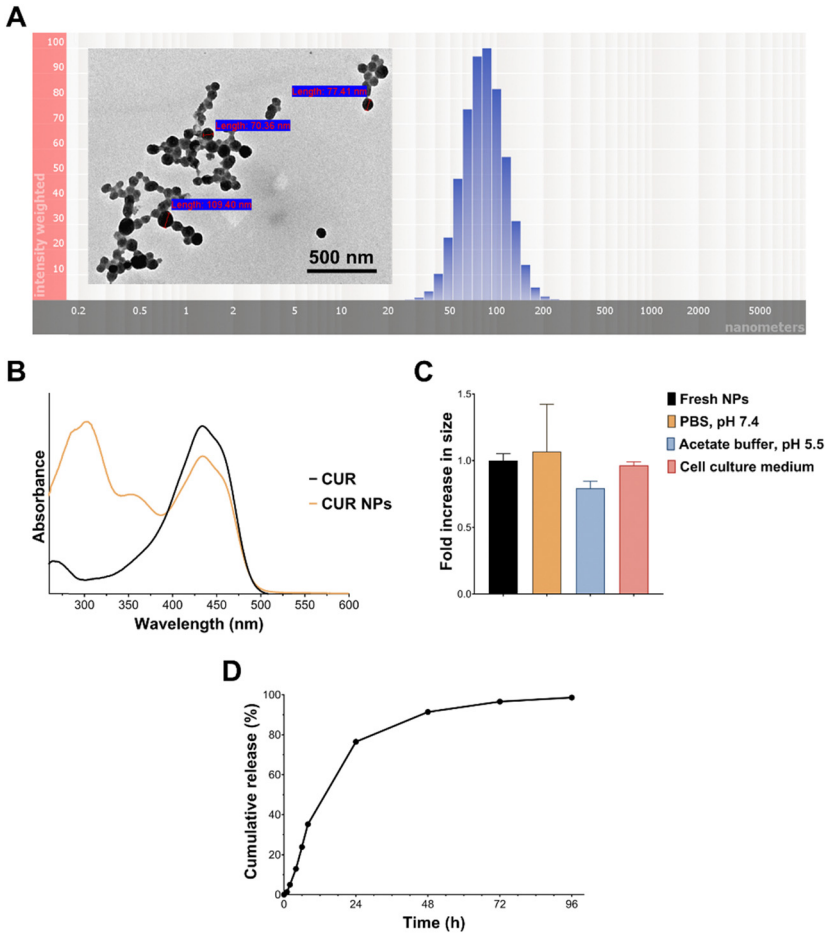

Fig. 2 (A) Representative TEM image and particle size distribution of CUR NPs; (B) UV-Vis spectrum of free CUR and CUR NPs; (C) colloidal stability of CUR NPs in the presence of buffers of different pH and serum-supplemented cell culture media. Results are expressed as the fold increase in size relative to fresh NPs (mean ± SD; n = 3) and showed no significant differences based on 1-way ANOVA followed by Tukey's *post hoc* test; (D) *in vitro* release profile of CUR NPs in PBS pH 7.4 and 37 °C.

Antiproliferative activity of CUR-loaded NPs

CUR has well-documented anticancer activity against a variety of cancer types, including breast cancer.[46,47] Here, we employed MCF-7 cells, a commonly used *in vitro* model for hormone receptor-positive breast cancer cells, to test the antiproliferative activity of CUR NPs. Cells were treated with various concentrations of CUR, CUR NPs, and blank NPs for 24, 48, and 72 h, followed by performing a cell viability assay. As presented in Fig. 3(A)–(C), all agents including blank NPs exhibited dose- and time-dependent reduction in cell viability. Notably, at 72 h (Fig. 3(C)), CUR NPs were significantly more toxic than free CUR at 10 μM ($p < 0.0001$; mean difference = 41.4; 95% confidence interval [38.0, 44.8]), and more toxic than blank NPs at 100 μM ($p < 0.0001$; mean difference = 6.9; 95% confidence interval [3.5, 10.2]). At the highest concentration of 300 μM, CUR NPs and blank NPs demonstrated an equal effect, whereas free CUR had the lowest effect on cell viability ($p < 0.001$). Upon fitting the 72 h cell viability data by nonlinear regression, the half-maximal inhibitory concentration (IC_{50}) could be determined, which reflects the potency of each treatment. Free CUR was associated with an IC_{50} of 24.3 μM, consistent with our previous findings.[25] Blank NPs demonstrated considerable antiproliferative activity, with an estimated IC_{50} of 241.5 μM oxQCT/TPGS. On the other hand, CUR NPs achieved an IC_{50} of 5.7 μM in terms of CUR and 57.8 μM in terms of the oxQCT/TPGS NP vehicle, denoting a marked increase in potency for both the free drug and the NPs. Applying the Chou–Talalay equation (eqn (3)) resulted in a CI of 0.47, which confirms synergism between CUR and the NP vehicle.

To further probe the anticancer activity of CUR and CUR NPs, a mitochondrial membrane potential assay was performed by relying on the conformational differences of the JC-1 probe in healthy and depolarized mitochondria. In healthy cells, JC-1 exists as aggregates that emit red fluorescence and are confined to the mitochondria. In cells undergoing apoptosis, depolarization of the mitochondria causes the aggregates to dissociate into monomers that emit green fluorescence as they exit into the cytosol.[48] Consequently, the ratio of the JC-1 monomer/aggregate fluorescence intensities serves as a measure of apoptosis induction. MCF-7 cells were treated with free CUR and equivalent concentrations of CUR NPs and blank NPs for 24 h, followed by JC-1 staining. The results shown in Fig. 3(D)

Open Access Article. Published on 14 February 2025. Downloaded on 4/6/2026 10:12:05 PM.
This article is licensed under a Creative Commons Attribution-NonCommercial 3.0 Unported Licence.

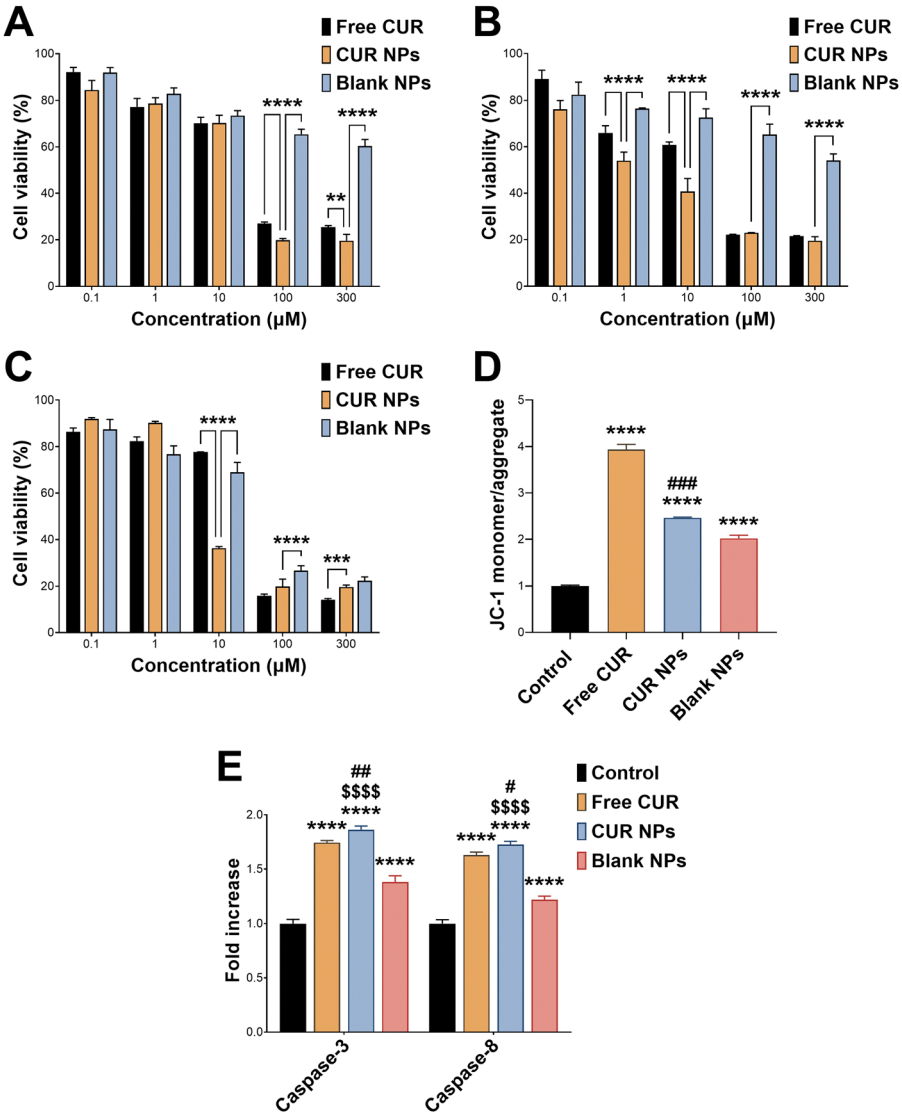

Fig. 3 Cell viability as a function of concentration after treating MCF-7 cells with free CUR, CUR NPs, and blank NPs (mean ± SD; n = 5) for (A) 24 h, (B) 48 h, and (C) 72 h. $^{**}p < 0.01$, $^{***}p < 0.001$, and $^{****}p < 0.0001$ based on 1-way ANOVA followed by Tukey's *post hoc* test; (D) JC-1 staining of MCF-7 cells treated with free CUR, CUR NPs, or blank NPs for 24 h expressed as the fold increase in JC-1 monomer/aggregate (green/red fluorescence) ratio relative to the control (mean ± SD; n = 3). $^{****}p < 0.0001$ compared to the control, and $^{###}p < 0.001$ compared to blank NPs based on 1-way ANOVA followed by Tukey's *post hoc* test; (E) levels of caspase-3 and caspase-8 in MCF-7 cells treated with free CUR, CUR NPs, or blank NPs for 24 h expressed as fold increase in each caspase level relative to the control (mean ± SD; n = 3). $^{****}p < 0.0001$ compared to the control, $^{\#}p < 0.05$ and $^{\#\#}p < 0.01$ compared to free CUR, $^{\$\$}p < 0.0001$ compared to blank NPs based on 1-way ANOVA followed by Tukey's *post hoc* test.

confirmed the proapoptotic activity of CUR which resulted in a 3.9-fold rise in JC-1 monomer/aggregate ratio compared to the control ($p < 0.0001$; mean difference = −2.9; 95% confidence interval [−3.1, −2.8]). Treatment with CUR NPs also resulted in a significant increase in JC-1 monomer/aggregate ratio of 2.5-fold compared to the control ($p < 0.0001$; mean difference = −1.5; 95% confidence interval [−1.6, −1.3]), although it was lower than the free drug. Nonetheless, CUR NPs maintained a greater increase in JC-1 monomer/aggregate ratio compared to blank NPs ($p < 0.001$; mean difference = 0.4; 95% confidence interval [0.3, 0.6]), which also demonstrated notable proapoptotic activity with a 2.0-fold increase relative to the control ($p < 0.0001$; mean difference = −1.0; 95% confidence interval [−1.2, −0.8]). These findings prompted a further investigation of caspases commonly upregulated in cells undergoing apoptosis such as caspase-3 and caspase-8. As shown in Fig. 3(E), all treatments including blank NPs promoted the expression of both caspase-3 and caspase-8. Importantly, CUR NPs were associated with a more significant increase in both caspases compared to the free drug ($p < 0.01$ and $p < 0.05$ in the case of caspase-3 and caspase-8, respectively), confirming the proapoptotic activity of the NPs, and that the NP vehicle synergizes with CUR in promoting cancer cell death.

The enhanced anticancer effects of CUR-loaded NPs compared to the free drug could be attributed to the inherent antiproliferative activity of the oxQCT/TPGS NP vehicle. This,

© 2025 The Author(s). Published by the Royal Society of Chemistry

Open Access Article. Published on 14 February 2025. Downloaded on 4/6/2026 10:12:05 PM.
This article is licensed under a Creative Commons Attribution-NonCommercial 3.0 Unported Licence.

in turn, is ascribed to the presence of TPGS, as oxQCT by itself has shown limited cytotoxicity against cancer[24,49] and normal cells.[30] Previous studies have reported on the anticancer activity of TPGS and TPGS-modified nanocarriers against a variety of cell types. For example, TPGS demonstrated time- and concentration-dependent cytotoxicity against wild-type MCF-7 and doxorubicin-resistant MCF-7/ADR cells. This effect was correlated with mitochondrial damage mediated by increased intracellular Ca^{2+} and cell cycle arrest in the G2/M phase, leading to apoptosis.[50] Furthermore, TPGS-modified bilosomes (bile salt-based vesicles) entrapping CUR displayed an increase in cytotoxicity compared to the plain bilosomes in MCF-7/ADR cells.[51] TPGS-polycaprolactone NPs also enhanced the bioactivity of paclitaxel against MCF-7 cells,[52] and resveratrol against 4T1 breast cancer cells.[53]

Uptake of CUR NPs by MCF-7 cells

Uptake experiments were performed to determine whether cellular uptake could contribute to the enhanced antiproliferative and proapoptotic activity of CUR NPs. As presented in Fig. 4, MCF-7 cells treated with free CUR up to 4 h exhibited moderate fluorescence, indicating that some CUR was able to internalize into the cell membrane, most likely by passive diffusion. On the other hand, cells treated with CUR NPs demonstrated significantly enhanced fluorescence at both time points as observed by fluorescence microscopy and quantified by flow cytometry, denoting a greater degree of internalization compared to the free drug. The NPs were most likely internalized by endocytosis, similar to other types of polymeric NPs.[54] Consequently, the superior anticancer activity of CUR NPs may in part be attributed to the promotion of cellular uptake by the NP formulation.

Anti-inflammatory activity of CUR-loaded NPs

The anti-inflammatory activity of CUR is mainly attributed to its antioxidant activity and its ability to scavenge reactive species and relieve oxidative stress associated with inflammation.[5,55] In this work, CUR was incorporated in TPGS-modified oxQCT NPs, where the NP vehicle itself also possesses antioxidant properties. oxQCT is derived from a potent antioxidant and maintains some antioxidant activity after partial oxidation,[30] while TPGS displays antioxidant properties due to the vitamin E component.[56] The antioxidant activity of CUR, CUR NPs, and blank NPs was experimentally determined by conducting a DPPH radical scavenging assay. As shown in Fig. 5(A), loading CUR in the NPs significantly enhanced its radical scavenging properties starting from 25 μM up to 100 μM ($p < 0.0001$), which suggests that the NP vehicle based on oxQCT and TPGS could also enhance the anti-inflammatory activity compared to the free drug. To test this hypothesis, an intracellular ROS assay was performed in LPS-stimulated RAW 264.7 macrophages using the DCFDA probe. This macrophage cell line was chosen as an *in vitro* model for inflammation for its consistent inflammatory response when challenged by stimulants such as LPS.[57]

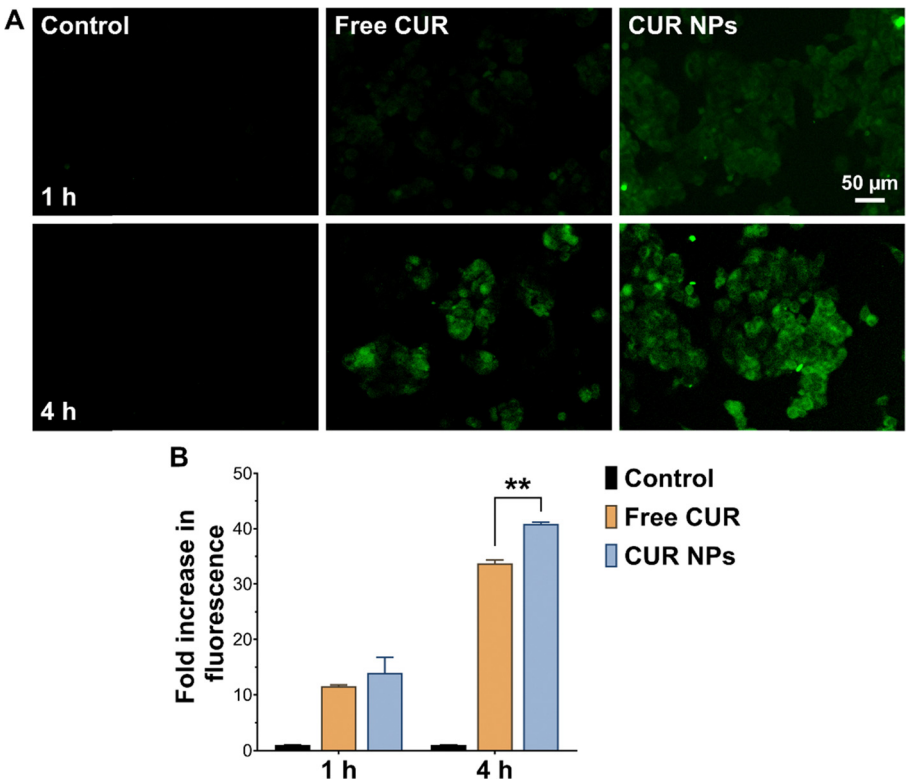

Fig. 4 (A) Fluorescence microscopy images and (B) quantified cell-associated fluorescence of MCF-7 cells incubated with free CUR or CUR NPs for 1 and 4 h showing significantly higher uptake in cells treated with CUR NPs compared to free CUR after 4 h of incubation. **$p < 0.01$ compared to free CUR ($n = 3$) based on 1-way ANOVA followed by Tukey's *post hoc* test.

Open Access Article. Published on 14 February 2025. Downloaded on 4/6/2026 10:12:05 PM.
This article is licensed under a Creative Commons Attribution-NonCommercial 3.0 Unported Licence.

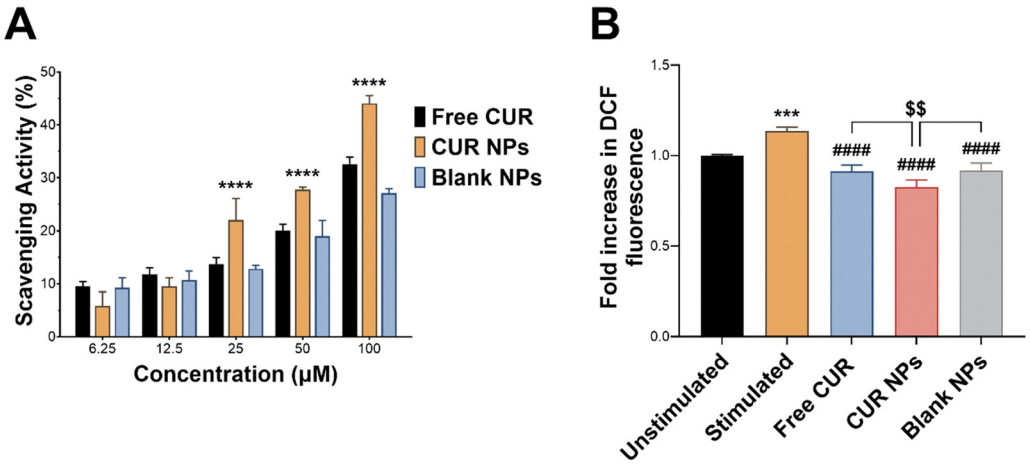

Fig. 5 (A) Antioxidant activity of free CUR, CUR NPs, and blank NPs measured by a DPPH radical scavenging assay, showing a significant improvement in CUR's radical scavenging activity in the form of CUR NPs. Results are expressed as scavenging activity % (mean ± SD; $n = 3$). ****$p < 0.0001$ compared to free CUR based on 1-way ANOVA followed by Tukey's *post hoc* test; (B) intracellular ROS measured by DCFDA in LPS-stimulated RAW 264.7 macrophages treated with free CUR, CUR NPs, and blank NPs. CUR NPs were superior to free CUR and the blank NPs in reducing intracellular ROS. Results are expressed as the fold increase in DCF fluorescence relative to unstimulated cells (mean ± SD; $n = 3$). ***$p < 0.001$ compared to unstimulated cells, $^{\#\#\#\#}p < 0.0001$ compared to LPS-stimulated cells, and $^{\$\$}p < 0.01$ compared to free CUR and blank NPs based on 1-way ANOVA followed by Tukey's *post hoc* test.

LPS stimulation increased intracellular ROS in macrophages by causing a significant rise in DCF fluorescence compared to the unstimulated cells (Fig. 5(B); $p < 0.001$). Co-treating the cells with LPS and free CUR, CUR NPs, or blank NPs significantly reduced intracellular ROS compared to LPS alone ($p < 0.0001$), which aligns with the DPPH assay and confirms the antioxidant properties of free CUR and the NPs. Interestingly, treatment with free CUR, CUR NPs, and blank NPs also relieved intrinsic oxidative stress in untreated unstimulated cells as indicated by the reduction in DCF fluorescence ($p < 0.05$, $p < 0.0001$, and $p < 0.05$, respectively). Importantly, CUR NPs demonstrated a superior ability to alleviate oxidative stress in LPS-stimulated macrophages compared to free CUR and blank NPs ($p < 0.01$), further supporting the ability of the NPs to potentiate the bioactivity of CUR.

The anti-inflammatory activity of CUR NPs was further investigated by measuring the proinflammatory cytokines TNF-α, IL-1β, and IL-6 released from LPS-stimulated macrophages. LPS is a potent toxin known to activate immune cells, which in turn secrete proinflammatory cytokines initiating an inflammatory cascade. This action was evident by the significant increase in secreted TNF-α, IL-1β, and IL-6 by LPS-stimulated RAW 264.7 macrophages compared to unstimulated cells (Fig. 6; $p < 0.0001$). In the case of TNF-α (Fig. 6(A)), co-treating the cells with LPS and CUR, CUR NPs, or blank NPs attenuated the increase in TNF-α secretion to varying degrees, with CUR NPs demonstrating the lowest level of TNF-α compared to free CUR ($p < 0.001$) and blank NPs ($p < 0.0001$). The same trend was observed in IL-1β levels (Fig. 6(B)), where free CUR, CUR NPs, and blank NPs inhibited IL-1β secretion upon LPS stimulation, and CUR NPs exhibited significantly lower levels compared to free CUR ($p < 0.01$) and blank NPs ($p < 0.0001$). As for IL-6 (Fig. 6(C)), co-treating the stimulated cells with free CUR completely normalized its levels. Although CUR NPs and blank NPs demonstrated statistically higher IL-6 levels compared to the unstimulated cells, no significant difference was detected between them and free CUR. The results of the DPPH, DCFDA, and cytokine assays collectively emphasize the potent anti-inflammatory activity of CUR NPs, and present oxQCT/TPGS NPs as a viable delivery platform that could potentiate CUR's action in inflammatory conditions. Our findings are aligned with previous reports which described the enhanced antioxidant and anti-inflammatory activity of CUR when formulated in inherently-antioxidant nanocarriers such as those derived from green tea polyphenols.[58,59]

Uptake of CUR NPs by RAW 264.7 macrophages

The superior anti-inflammatory activity of CUR NPs could in part be attributed to the inherent antioxidant properties of the NP vehicle itself. To determine whether cellular uptake may have also played a role as in the case of MCF-7 cells, RAW 264.7 macrophages were imaged by fluorescence microscopy and analyzed by flow cytometry following treatment with free CUR and CUR NPs. Consistent with the uptake results in MCF-7 cells (Fig. 4), the macrophages internalized CUR NPs more readily than free CUR, as evidenced by more prominent fluorescence signals particularly at 4 h (Fig. 7).

SR-μFTIR measurements of MCF-7 cells and RAW 264.7 macrophages upon treatment with CUR NPs

In this study, we employed SR-μFTIR to further investigate the anticancer and anti-inflammatory activities of CUR in the developed NP formulation. Two main IR spectral regions were defined and investigated as reported previously.[40] The first region (3050–2800 cm^{-1}) corresponds to the distribution of lipids, while the second region (1855–1485 cm^{-1}) corresponds to the

© 2025 The Author(s). Published by the Royal Society of Chemistry

Open Access Article. Published on 14 February 2025. Downloaded on 4/6/2026 10:12:05 PM.
This article is licensed under a Creative Commons Attribution-NonCommercial 3.0 Unported Licence.

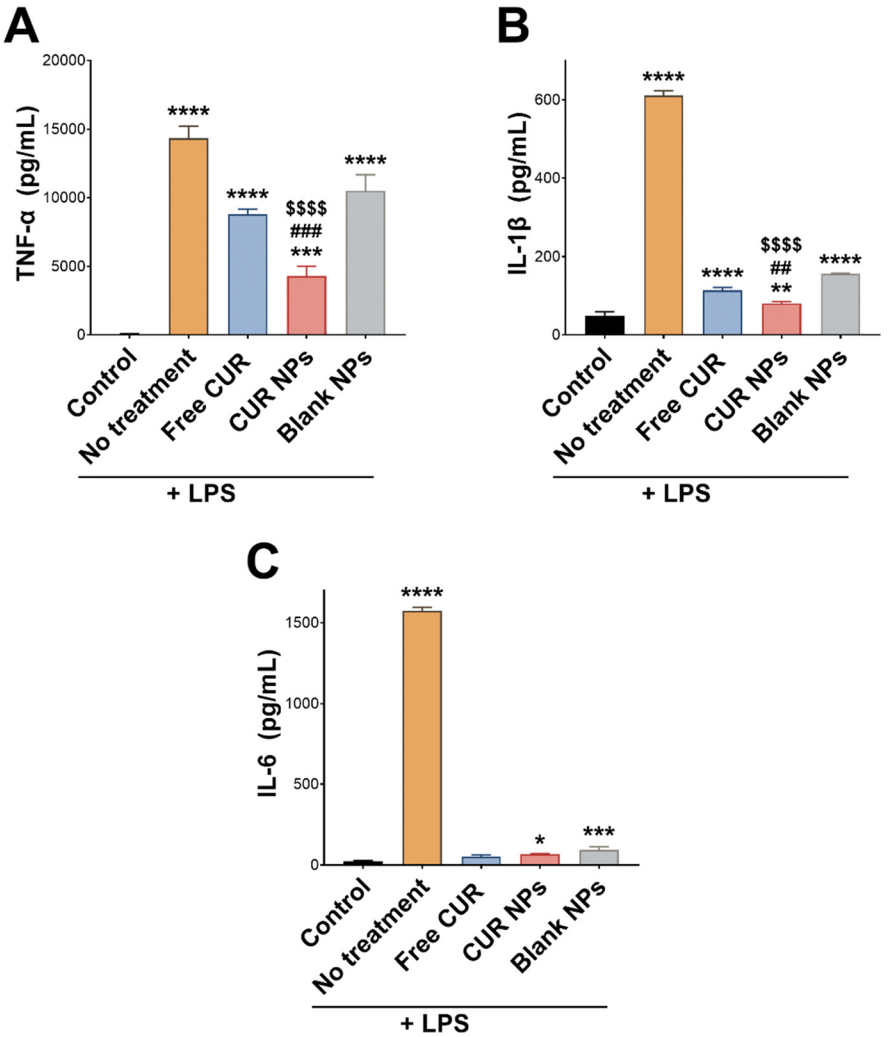

Fig. 6 Levels of (A) TNF-α, (B) IL-1β, and (C) IL-6 proinflammatory cytokines secreted by LPS-stimulated RAW 264.7 macrophages following treatment with free CUR, CUR NPs, and blank NPs. CUR NPs exhibited a marked reduction in TNF-α and IL-1β levels and a similar effect on IL-6 levels compared to free CUR. Results are expressed as the mean concentration of each cytokine ± SD (n = 3). *$p < 0.05$, **$p < 0.01$, ***$p < 0.001$, and ****$p < 0.0001$ compared to unstimulated cells, $^{\#\#}p < 0.01$ and $^{\#\#\#}p < 0.001$ compared to cells treated with free CUR, and $^{\$\$}p < 0.0001$ compared to blank NPs based on 1-way ANOVA followed by Tukey's *post hoc* test.

distribution of carbonyl (1855–1700 cm^{-1}) and protein bands amide I (1700–1600 cm^{-1}) and amide II (1600–1485 cm^{-1}).[60] Note that sample thickness and homogeneity, IR slides, and fixation methods used during sample preparation can all influence the reproducibility and the quality of the obtained IR spectra. In the current work, a standardized published sample preparation protocol was applied to minimize the effect of sample preparation.[28] CaF_2 IR transmission windows were selected as the growing surface due to their compatibility with IR and their ability to provide excellent cell adherence. The cell volume was carefully optimized to ensure the formation of a homogeneous, monolayer thin film. Fixation was performed using paraformaldehyde, which offers minimal interference in the IR spectrum, ensures uniform fixation, and effectively preserves key biomolecules including lipids and proteins.

Lipid and protein alterations in MCF-7 cells. For the lipid region, the PCA score plots (Fig. 8(A)) showed an evident and clear separation, reflecting spectral changes in the lipid region between the four groups (control, free CUR, CUR NPs, and blank NPs). Principal component (PC)-1 and PC-2 described 94% of the variability in the data. The loadings of PC-1 and PC-2 of the PCA model (Fig. S1 of the ESI†) revealed that the most important discriminative variables for PC-1 in MCF-7 cells were 2916 and 2848.6 cm^{-1}, corresponding to $asCH_2$ (asymmetric) and $symCH_2$ (symmetric) stretching vibrations, respectively. When comparing the average raw spectra of the different groups (Fig. 8(C) and Table 2), the lipid region spectrum for blank NPs highly overlapped with the spectrum corresponding to the control group, exhibiting similar peak intensities for $asCH_3$, $asCH_2$, $symCH_3$, and $symCH_2$ stretching vibrations. Cells treated with free CUR were associated with an increase in the absorbance signal in the $asCH_3$ region, and a decrease in the signal intensity of as- and $symCH_2$ stretching vibrations compared to the control. On the other hand, CUR NPs showed a

Open Access Article. Published on 14 February 2025. Downloaded on 4/6/2026 10:12:05 PM.
This article is licensed under a Creative Commons Attribution-NonCommercial 3.0 Unported Licence.

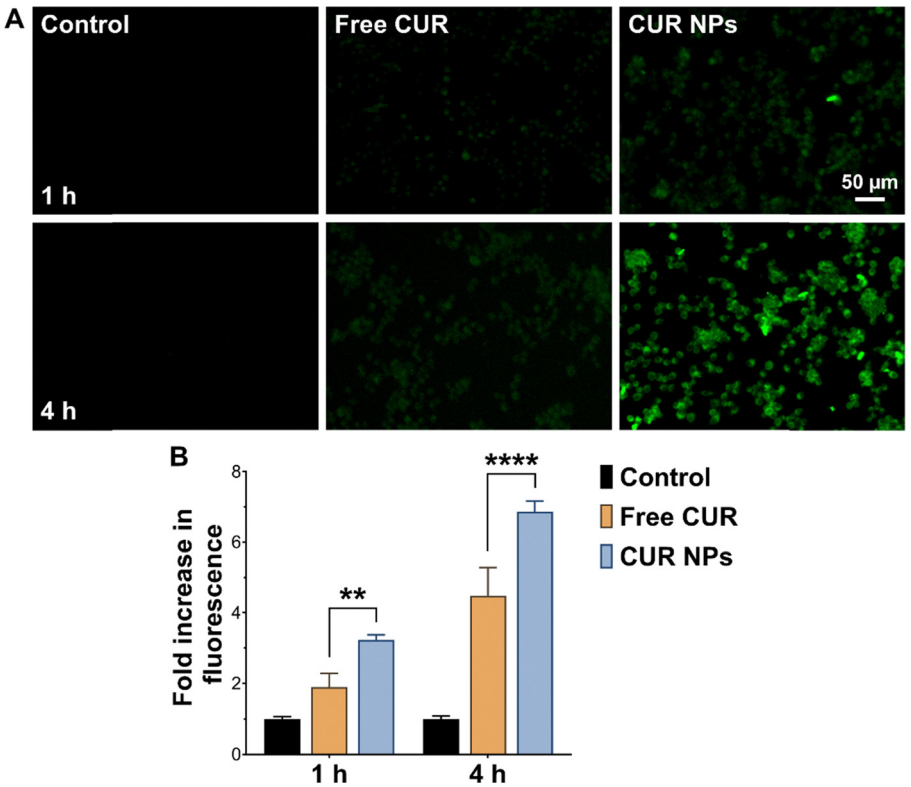

Fig. 7 (A) Fluorescence microscopy images and (B) quantified cell-associated fluorescence of RAW 264.7 macrophages incubated with free CUR or CUR NPs for 1 and 4 h. CUR NPs demonstrated significantly higher cellular uptake compared to free CUR. $^{**}p < 0.01$ and $^{****}p < 0.0001$ compared to free CUR (n = 3) based on 1-way ANOVA followed by Tukey's *post hoc* test.

decrease in the absorbance signals of as- and symCH_3 and an increase in the as- and symCH_2 peaks (Table 2). CH_3 and CH_2 stretching vibrations correspond to cholesterol esters and triglycerides, and long chain fatty acids and phospholipids, respectively.[61] The observed changes in peak intensities may suggest significant changes in the lipid profile in the treated cells. Besides the changes in peak intensities, free CUR caused a blue shift in the asCH_2 peak (2924 cm^{-1}) compared to the control (2918 cm^{-1}; Table 2), This shift to a higher wavenumber might indicate a change in the lipid composition of the cell membrane, as asCH_2 stretching is associated with phospholipid and long chain fatty acids. The CH_2/CH_3 ratio can be used to estimate lipid unsaturation. A higher ratio indicates a high content of unsaturated fatty acids, which might point to abnormalities in physical properties, fluidity and permeability of the cell membrane, structural variations of lipids, and conformational changes in lipid tails.[62] Given that as- and symCH_2 stretching vibrations provide information about the order of hydrocarbon tails in lipids, an increase in the CH_2/CH_3 ratio suggested conformational changes in the order of lipid acyl chains.[62] As shown in Table 3, treatment with free CUR caused a reduction in the CH_2/CH_3 ratio compared to the control, denoting decreased levels of lipid unsaturation and increased membrane rigidity. Conversely, cells treated with CUR NPs and blank NPs exhibited an increase in the CH_2/CH_3 ratio, which may suggest an increase in cell membrane fluidity.[63] This aligns with the cellular uptake experiment (Fig. 4) which showed that CUR NPs were more easily internalized by MCF-7 cells. Therefore, the increase in membrane fluidity due to a change in the ratio of unsaturated/saturated lipids may have contributed to the enhanced cellular uptake of CUR NPs.

As for the protein-carbonyl region, the PCA score plots also revealed a good separation of the groups (Fig. 8(B)). PC-1 and PC-2 loading of the second derivative protein region (Fig. S1 of the ESI†) was characterized by strong peaks in the area of amide I and amide II. The average raw spectra (Fig. 8(D)) revealed similar signal intensities of amide I and amide II between free CUR and the control. While the blank NPs showed a small increase in amide I and amide II signals, CUR NPs exhibited a decrease in amide I and an increase in amide II signals (more than blank NPs) compared to the control (Table 2). Upon examination of the second derivative spectra of the protein-carbonyl region (Fig. 8(E)), we found that amide I had the strongest signal in the loading plot and, hence, the most important variable for group separation. As seen in Fig. 8(E), the amide I signal at 1650.9 cm^{-1} in the control, blank and CUR NPs groups was shifted to 1652.9 cm^{-1} in the free CUR group (Table 2), denoting a possible conformational change in the α-helix protein secondary structure.[64,65] Generally, spectral analysis of the protein region revealed that CUR NPs mainly affected the protein profile but had no significant effect on the protein conformation in MCF-7 cells. With regard to the

© 2025 The Author(s). Published by the Royal Society of Chemistry

Open Access Article. Published on 14 February 2025. Downloaded on 4/6/2026 10:12:05 PM.
This article is licensed under a Creative Commons Attribution-NonCommercial 3.0 Unported Licence.

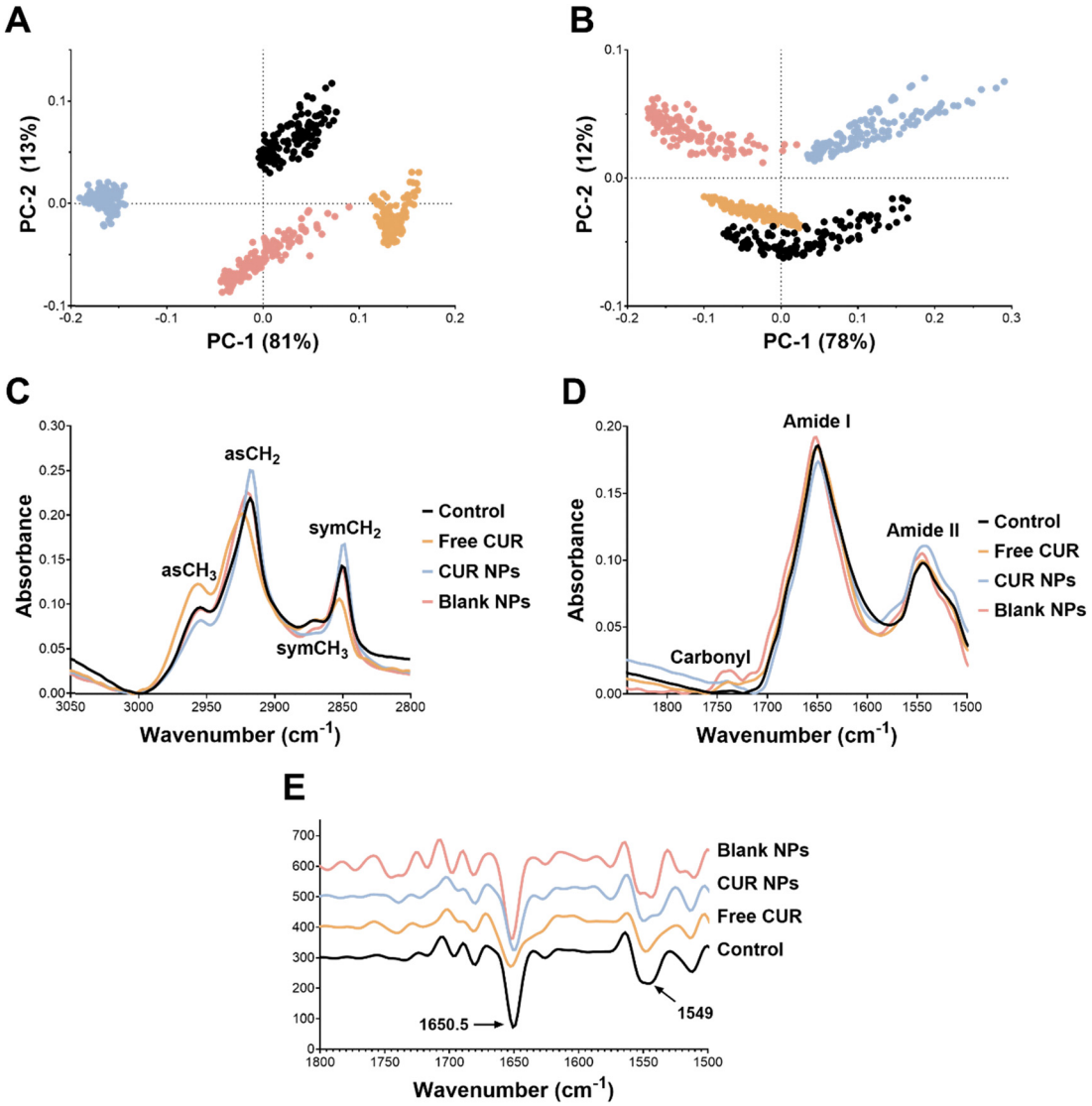

Fig. 8 SR-μFTIR measurements of the lipid and protein-carbonyl regions in MCF-7 cells. PCA-score plots of the (A) lipid and (B) protein-carbonyl regions. Control: black dots; free CUR: orange dots; CUR NPs: blue dots; blank NPs: pink dots; unit vector normalized average raw spectra of the (C) lipid and (D) protein-carbonyl regions; (F) normalized reduced Savitsky–Golay second derivative average spectra of the protein-carbonyl region.

Table 2 Peak assignments of lipids, amide I, amide II, and carbonyl bands in MCF-7 cells and their alterations upon treatment with free CUR, CUR NPs, or blank NPs

Wavenumber (cm^{-1})	Structure	Alterations compared to the control
2955.5	$asCH_3$: cholesterol esters, triglycerides	Free CUR: increase in signal intensity CUR NPs: decrease in signal intensity
2918.0	$asCH_2$: long chain fatty acids, phospholipids	Free CUR: decrease in signal intensity; blue shift to 2924 cm^{-1} CUR NPs: increase in signal intensity
2872.8	$symCH_3$: cholesterol esters, triglycerides	CUR NPs: decrease in signal intensity
2850.0	$symCH_2$: long chain fatty acids, phospholipids	Free CUR: decrease in signal intensity CUR NPs: increase in signal intensity
1650.9	Amide I, α-helix	Free CUR: blue shift to 1652.9 cm^{-1} CUR NPs: decrease in signal intensity Blank NPs: increase in signal intensity
1544.5	Amide II, α-helix	CUR NPs: increase in signal intensity Blank NPs: increase in signal intensity (less than CUR NPs)
1740.0	Lipid carbonyl	Increase in signal intensity in all groups compared to the control

Open Access Article. Published on 14 February 2025. Downloaded on 4/6/2026 10:12:05 PM.
This article is licensed under a Creative Commons Attribution-NonCommercial 3.0 Unported Licence.

Table 3 CH_2/CH_3 ratio derived from the unit vector normalized average raw spectra of the lipid regions in MCF-7 cells treated with free CUR, CUR NPs, and blank NPs, and in RAW 264.7 macrophages stimulated with LPS and treated with free CUR, CUR NPs, and blank NPs

Cell line	Treatment	CH_2/CH_3
MCF-7	Control	2.06
	Free CUR	1.55
	CUR NPs	2.80
	Blank NPs	2.38
RAW 264.7	Control	1.55
	LPS	1.38
	Free CUR	2.06
	CUR NPs	1.33
	Blank NPs	2.53

carbonyl region, the three treatments (free CUR, CUR NPs, and blank NPs) caused an increase in the carbonyl signal at 1740 cm^{-1} (Fig. 8(D) and Table 2). This could be related to an increase in oxidative stress resulting from lipid peroxidation, which contributes to the apoptosis cascade.[66,67]

Lipid and protein alterations in LPS-stimulated RAW 264.7 macrophages. Similar to MCF-7 cells, the PCA score plots for the lipid and protein-carbonyl regions revealed a good separation of the different groups (Fig. 9(A) and (B)). In the lipid region, loading of the PC-1 and PC-2 variables showed that the most important discriminative variables for PC-1 were 2962, 2914 and 2847 cm^{-1}, corresponding to $asCH_3$, $asCH_2$ and $symCH_2$ stretching vibrations, respectively (Fig. S1 of the ESI†). Upon comparing the average raw spectra of the lipid region across the different groups (Fig. 9(C) and Table 4), cells treated

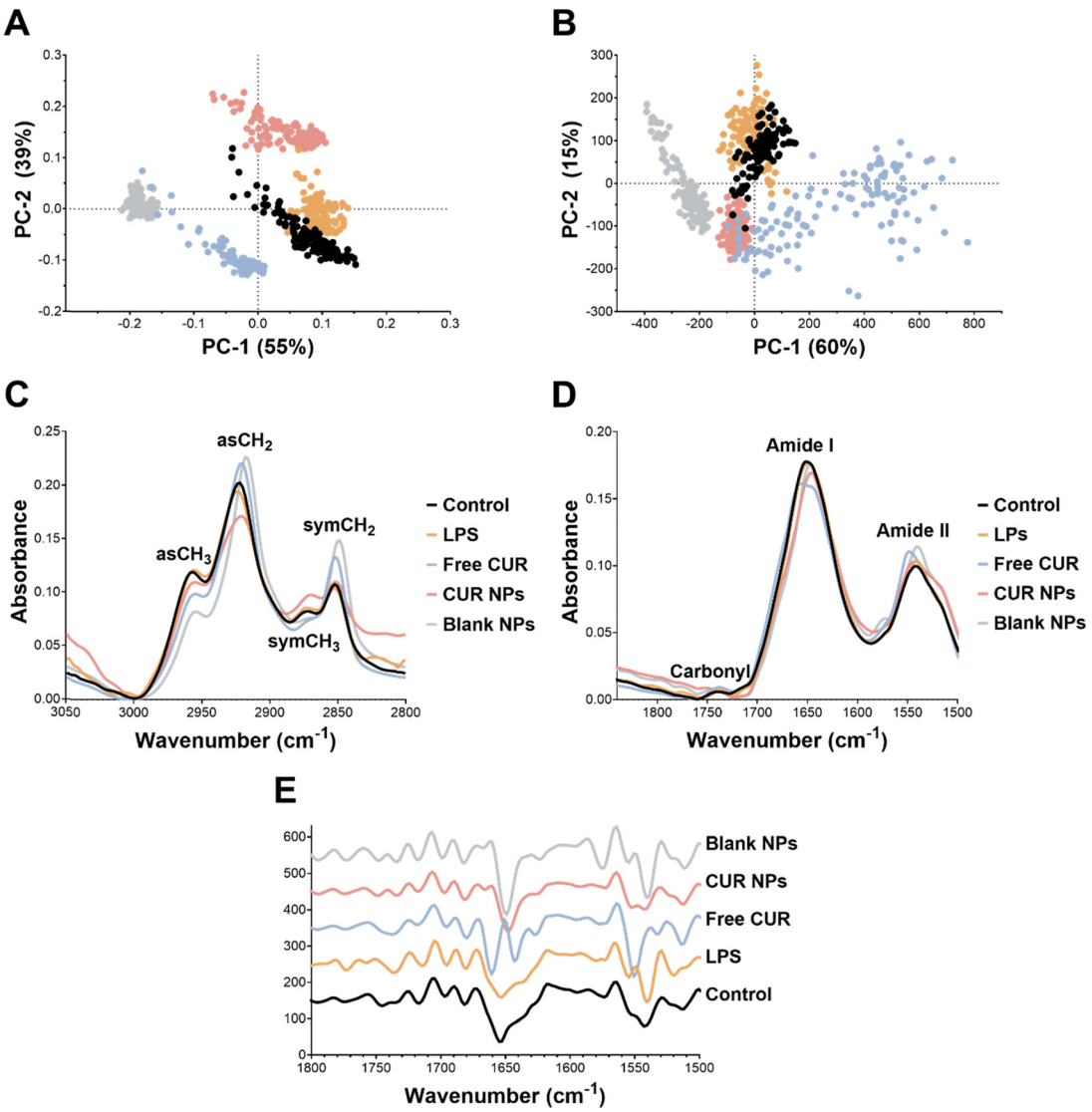

Fig. 9 SR-μFTIR measurements of the lipid and protein-carbonyl regions in RAW 264.7 macrophages. PCA-score plots of the (A) lipid and (B) protein-carbonyl regions. Control: black dots; LPS-stimulated cells: orange dots; free CUR: blue dots; CUR NPs: pink dots; blank NPs: grey dots; unit vector normalized average raw spectra of the (C) lipid and (D) protein-carbonyl regions; (F) normalized reduced Savitsky–Golay second derivative average spectra of the protein-carbonyl region.

© 2025 The Author(s). Published by the Royal Society of Chemistry

Open Access Article. Published on 14 February 2025. Downloaded on 4/6/2026 10:12:05 PM. This article is licensed under a Creative Commons Attribution-NonCommercial 3.0 Unported Licence.

Table 4 Peak assignments of lipids, amide I, amide II, and carbonyl bands in RAW 264.7 macrophages and their alterations upon treatment with free CUR, CUR NPs, or blank NPs

Wavenumber (cm^{-1})	Structure	Alterations compared to the control
2957.0	$asCH_3$: cholesterol esters, triglycerides	Free CUR, CUR NPs, and blank NPs: decrease in signal intensity
2921.9	$asCH_2$: long chain fatty acids, phospholipids	Free CUR: increase in signal intensity CUR NPs: decrease in signal intensity Blank NPs: increase in signal intensity; red shift to 2918 cm^{-1}
2873.4	$symCH_3$: cholesterol esters, triglycerides	Free CUR and blank NPs: decrease in signal intensity CUR NPs: increase in signal intensity
2852.4	$symCH_2$: long chain fatty acids, phospholipids	Free CUR: increase in signal intensity Blank NPs: increase in signal intensity; red shift to 2848.6 cm^{-1}
1650.9	Amide I, α-helix	Free CUR: decrease in signal intensity; blue shift to 1654.8 cm^{-1} CUR NPs: red shift to 1645.1 cm^{-1}
1541.0	Amide II, α-helix	Free CUR: increase in signal intensity; blue shift to 1548.9 cm^{-1}
1740.0	Lipid carbonyl	No difference between all groups

with free CUR, CUR NPs, and blank NPs were associated with a decrease in the absorbance signal in the $asCH_3$ region to varying degrees. Free CUR and the blank NPs both caused an increase in the absorbance of the as- and $symCH_2$ regions and a slight decrease in the signal intensity of $symCH_3$ compared to the control. CUR NPs resulted in a decrease in the absorbance signals of $asCH_2$ and an increase in the $symCH_3$ peak. These changes in peak intensities across the different treatment groups may correlate with changes in the lipid composition in the cells. Moreover, blank NPs resulted in an evident red shift in the $asCH_2$ peak and $symCH_2$ compared to the control (2921.9 and 2852.4 cm^{-1} in the control to 2918 and 2848.6 cm^{-1} in blank NPs, respectively). As for the CH_2/CH_3 ratio (Table 3), the most notable changes were observed in the blank NPs and the free CUR groups, where the ratio was increased from 1.55 (control) to 2.53 and 2.06, respectively, which suggests a significant change in the order of lipid acyl chains.

As for the protein-carbonyl region, PC-1 and PC-2 loading plots were characterized by strong amide I and amide II peaks (Fig. S1 of the ESI†). As observed in Fig. 9(D) and Table 4, Among the four groups, free CUR was associated with the most significant changes in the protein spectral region. In terms of signal intensities, the free CUR group exhibited a decrease and an increase in the peak intensities for the amide I and amide II signals compared to the control, respectively. Furthermore, the amide I peak in free CUR was shifted to 1654.8 cm^{-1} whereas the amide II peak was shifted to 1548.9 cm^{-1} compared to the control (1650.9 and 1541 cm^{-1}, respectively; Table 4). These findings suggest a possible change in the protein secondary structure (α-helix) to a less ordered structure upon treating the macrophages with free CUR.[68] These observations were further corroborated by the second derivative spectra of the protein-carbonyl region (Fig. 9(E)), where the free CUR group exhibited a notable change in the amide I peak compared to the control. Additionally, CUR NPs exhibited a shift in the amide I peak position to 1645.1 cm^{-1} compared to 1650.9 cm^{-1} in the control, suggesting a possible change in the protein secondary structure for amide I from α-helix in the control group to the unordered random coil conformation.[68] These spectral changes observed in free CUR and CUR NPs may correlate with cytokine secretion.

Taken together, SR-μFTIR analyses corroborated the diverse bioactivities of CUR as a function of the cell line, and how these bioactivities could be modulated by the developed delivery platform oxQCT/TPGS NPs. For example, in MCF-7 cells, most of the biochemical changes detected by SR-μFTIR were related to the lipid profile, suggesting a potential role in affecting plasma membrane permeability and/or lipid peroxidation as they relate to apoptotic events. In the macrophages, the most notable changes were related to the protein composition, which could be ascribed to alterations in cytokine secretion.

Conclusion

In this study, we prepared and characterized a novel nano-formulation for CUR based on an emerging nanocarrier, oxQCT. We showed that co-formulating oxQCT with TPGS significantly improves the anticancer and anti-inflammatory activities of CUR and promotes cellular uptake in MCF-7 and RAW 264.7 macrophages, respectively. MCF-7 cell death was mediated *via* a mitochondrial and caspase-dependent pathway. In RAW 264.7 macrophages, the NPs significantly attenuated the secretion of proinflammatory cytokines upon LPS stimulation. The promising *in vitro* results prompt further *in vivo* validation in appropriate animal models. Furthermore, SR-μFTIR measurements of the treated cell lines provided clues regarding the biochemical changes associated with CUR treatment, both as a free drug and as an NP formulation. This emphasizes the importance of advanced bioanalytical techniques in delineating the biological activities of new NP therapeutics, an important step toward their clinical translation.

Data availability

The data supporting this article have been included as part of the ESI.†

Conflicts of interest

There are no conflicts to declare.

Open Access Article. Published on 14 February 2025. Downloaded on 4/6/2026 10:12:05 PM. This article is licensed under a Creative Commons Attribution-NonCommercial 3.0 Unported Licence.

Acknowledgements

This work was supported by Al-Zaytoonah University of Jordan (grant no. 14/08/2021-2022) and the International Centre for Genetic Engineering and Biotechnology (ICGEB; contract no. CRP/22/006). The authors thank Dr Gihan Kamel (IR Beamline Principal Scientist at SESAME) for assistance with SR-μFTIR measurements.

References

1 J. Sharifi-Rad, Y. E. Rayess, A. A. Rizk, C. Sadaka, R. Zgheib, W. Zam, S. Sestito, S. Rapposelli, K. Neffe-Skocińska, D. Zielińska, B. Salehi, W. N. Setzer, N. S. Dosoky, Y. Taheri, M. El Beyrouthy, M. Martorell, E. A. Ostrander, H. A. R. Suleria, W. C. Cho, A. Maroyi and N. Martins, *Front. Pharmacol.*, 2020, **11**, 550909.
2 X.-Y. Xu, X. Meng, S. Li, R.-Y. Gan, Y. Li and H.-B. Li, *Nutrients*, 2018, **10**, 1553.
3 A. Allegra, V. Innao, S. Russo, D. Gerace, A. Alonci and C. Musolino, *Cancer Invest.*, 2017, **35**, 1–22.
4 M. E. Abd El-Hack, M. T. El-Saadony, A. A. Swelum, M. Arif, M. M. Abo Ghanima, M. Shukry, A. Noreldin, A. E. Taha and K. A. El-Tarabily, *J. Sci. Food Agric.*, 2021, **101**, 5747–5762.
5 Y. Peng, M. Ao, B. Dong, Y. Jiang, L. Yu, Z. Chen, C. Hu and R. Xu, *Drug Des., Dev. Ther.*, 2021, 4503–4525.
6 M. C. Fadus, C. Lau, J. Bikhchandani and H. T. Lynch, *J. Tradit. Complementary Med.*, 2017, **7**, 339–346.
7 S. Sabet, A. Rashidinejad, L. D. Melton and D. J. McGillivray, *Trends Food Sci. Technol.*, 2021, **110**, 253–266.
8 M. Kharat and D. J. McClements, *J. Colloid Interface Sci.*, 2019, **557**, 506–518.
9 Y. Chen, Y. Lu, R. J. Lee and G. Xiang, *Int. J. Nanomed.*, 2020, 3099–3120.
10 B. Salehi, M. L. Del Prado-Audelo, H. Cortés, G. Leyva-Gómez, Z. Stojanović-Radić, Y. D. Singh, J. K. Patra, G. Das, N. Martins and M. Martorell, *J. Clin. Med.*, 2020, **9**, 746.
11 S. Maleki Dizaj, M. Alipour, E. Dalir Abdolahinia, E. Ahmadian, A. Eftekhari, H. Forouhandeh, Y. Rahbar Saadat, S. Sharifi and S. Zununi Vahed, *Phytother. Res.*, 2022, **36**, 1156–1181.
12 J. Guo, T. Suma, J. J. Richardson and H. Ejima, *ACS Biomater. Sci. Eng.*, 2019, **5**, 5578–5596.
13 Z. Chen, M. A. Farag, Z. Zhong, C. Zhang, Y. Yang, S. Wang and Y. Wang, *Adv. Drug Delivery Rev.*, 2021, **176**, 113870.
14 X. Wang, Y. Fan, J. Yan and M. Yang, *Chem. Eng. J.*, 2022, **439**, 135661.
15 J. Zhou, Z. Lin, Y. Ju, M. A. Rahim, J. J. Richardson and F. Caruso, *Acc. Chem. Res.*, 2020, **53**, 1269–1278.
16 D. Wu, J. Zhou, M. N. Creyer, W. Yim, Z. Chen, P. B. Messersmith and J. V. Jokerst, *Chem. Soc. Rev.*, 2021, **50**, 4432–4483.
17 S. Xiang, P. Yang, H. Guo, S. Zhang, X. Zhang, F. Zhu and Y. Li, *Macromol. Rapid Commun.*, 2017, **38**, 1700446.
18 Z. Yi, G. Chen, X. Chen, X. Ma, X. Cui, Z. Sun, W. Su and X. Li, *ACS Appl. Mater. Interfaces*, 2020, **12**, 33550–33563.
19 Z. Yi, X. Chen, G. Chen, Z. Deng, Q. Tong, Z. Sun, X. Ma, W. Su, L. Ma, Y. Ran and X. Li, *ACS Appl. Mater. Interfaces*, 2020, **12**, 37914–37928.
20 P. Chowdhury, P. K. Nagesh, E. Hatami, S. Wagh, N. Dan, M. K. Tripathi, S. Khan, B. B. Hafeez, B. Meibohm and S. C. Chauhan, *J. Colloid Interface Sci.*, 2019, **535**, 133–148.
21 T. Wang, Q. Fan, J. Hong, Z. Chen, X. Zhou, J. Zhang, Y. Dai, H. Jiang, Z. Gu, Y. Cheng and Y. Li, *Small*, 2021, **17**, 2102485.
22 S. Sunoqrot, E. Al-Shalabi, A. G. Al-Bakri, H. Zalloum, B. Abu-Irmaileh, L. H. Ibrahim and H. Zeno, *ACS Omega*, 2021, **6**, 2767–2776.
23 S. Sunoqrot, A. G. Al-Bakri, L. H. Ibrahim and N. Aldaken, *ACS Appl. Bio Mater.*, 2022, **5**, 5156–5164.
24 S. Sunoqrot, E. Al-Shalabi and P. B. Messersmith, *Biomater. Sci.*, 2018, **6**, 2656–2666.
25 S. Sunoqrot, S. Abusulieh and O. H. Abusara, *Int. J. Pharm.*, 2023, **645**, 123392.
26 O. Alkhaldi, S. Abusulieh, O. H. Abusara and S. Sunoqrot, *Int. J. Pharm.*, 2024, **665**, 124674.
27 A. Refaat and G. Kamel, *Appl. Spectrosc. Rev.*, 2022, **58**, 525–544.
28 N. Elmadany, E. Khalil, L. Vaccari, G. Birarda, I. Yousef and R. Abu-Dahab, *Infrared Phys. Technol.*, 2018, **95**, 141–147.
29 B. Dunkhunthod, C. Talabnin, M. Murphy, K. Thumanu, P. Sittisart, T. Hengpratom and G. Eumkeb, *J. Evidence-Based Complementary Altern. Med.*, 2020, **1**, 7436920.
30 S. Sunoqrot, E. Al-Shalabi, L. Hasan Ibrahim and H. Zalloum, *Molecules*, 2019, **24**, 3815.
31 R. W. Korsmeyer, R. Gurny, E. Doelker, P. Buri and N. A. Peppas, *Int. J. Pharm.*, 1983, **15**, 25–35.
32 J. Siepmann and N. A. Peppas, *Adv. Drug Delivery Rev.*, 2012, **64**, 163–174.
33 T.-C. Chou, *Pharmacol. Rev.*, 2006, **58**, 621–681.
34 N. N. Mahmoud, R. Abu-Dahab, L. A. Hamadneh, D. Abuarqoub, H. Jafar and E. A. Khalil, *Mol. Pharmaceutics*, 2019, **16**, 4149–4164.
35 A. R. Althaher, S. A. Oran, M. W. Awadallah, H. H. Ameen, R. F. Shehabi, L. M. S. Bourghli and A. Mastinu, *Chem. Biodiversity*, 2024, **21**, e202400026.
36 E. Al-Shalabi, S. Abusulieh, A. M. Hammad and S. Sunoqrot, *Biomater. Sci.*, 2022, **10**, 5504–5519.
37 S. Sunoqrot, M. Alkurdi, A. Q. Al Bawab, A. M. Hammad, R. Tayyem, A. Abu Obeed and M. Abufara, *Saudi Pharm. J.*, 2023, **31**, 845–853.
38 G. Kamel, S. Lefrançois, M. Al-Najdawi, T. Abu-Hanieh, I. Saleh, Y. Momani and P. Dumas, *Synchrotron Radiat. News*, 2017, **30**, 8–10.
39 G. Kamel, S. Lefrancois, T. Moreno, M. Al-Najdawi, Y. Momani, A. Abbadi, G. Paolucci and P. Dumas, *J. Synchrotron Radiat.*, 2021, **28**, 1927–1934.
40 L. A. Dahabiyeh, R. S. H. Mansour, S. S. Saleh and G. Kamel, *J. Pharm. Biomed. Anal.*, 2020, **184**, 113186.
41 R. Nimer, G. Kamel, M. A. Obeidat and L. A. Dahabiyeh, *Spectrochim. Acta, Part A*, 2022, **264**, 120259.
42 L. A. Dahabiyeh, R. S. Mansour, W. Darwish, S. S. Saleh and G. Kamel, *J. Pharm. Biomed. Anal.*, 2022, **220**, 114981.

© 2025 The Author(s). Published by the Royal Society of Chemistry

Open Access Article. Published on 14 February 2025. Downloaded on 4/6/2026 10:12:05 PM.
This article is licensed under a Creative Commons Attribution-NonCommercial 3.0 Unported Licence.

43 A. G. Al-Bakri, L. A. Dahabiyeh, E. Khalil, D. Jaber, G. Kamel, N. Schleimer, C. Kohler and K. Becker, *Antibiotics*, 2022, **11**, 1607.
44 D. Liu, X. Chen, Z. Yi, Q. Tong, L. Ma, Y. Tan, X. Cao and X. Li, *ACS Appl. Bio Mater.*, 2024, **7**, 1763–1777.
45 S. Rathod, P. Bahadur and S. Tiwari, *Int. J. Pharm.*, 2021, **592**, 120045.
46 V. Zoi, V. Galani, G. D. Lianos, S. Voulgaris, A. P. Kyritsis and G. A. Alexiou, *Biomedicines*, 2021, **9**, 1086.
47 K. A. Barcelos, C. R. Mendonça, M. Noll, A. F. Botelho, C. R. D. Francischini and M. A. M. Silva, *Cancers*, 2022, **14**, 2165.
48 F. Sivandzade, A. Bhalerao and L. Cucullo, *Bio-Protoc.*, 2019, **9**, e3128.
49 S. Sunoqrot, T. Al-Debsi, E. Al-Shalabi, L. Hasan Ibrahim, F. N. Faruqu, A. Walters, R. Palgrave and K. T. Al-Jamal, *ACS Biomater. Sci. Eng.*, 2019, **5**, 6036–6045.
50 L. Tang, K. Huang, W. Jiang, L. Fu, R. Zhang, L. Shen, Z. Ou, Y. Huang and Z. Zhang, *Drug Delivery*, 2023, **30**, 2183830.
51 H. Hegazy, M. M. Amin, W. Fayad and M. Y. Zakaria, *Int. J. Pharm.*, 2022, **619**, 121717.
52 T. Chen, F. Xing and Y. Sun, *J. Exp. Nanosci.*, 2024, **19**, 2281938.
53 P. G. Cavalcante de Freitas, B. Rodrigues Arruda, M. G. Araújo Mendes, J. V. Barroso de Freitas, M. E. da Silva, T. L. Sampaio, R. Petrilli and J. O. Eloy, *Cancers*, 2023, **15**, 2802.
54 L. C. Nelemans and L. Gurevich, *Materials*, 2020, **13**, 366.
55 K. Mokgalaboni, Y. Ntamo, K. Ziqubu, T. M. Nyambuya, B. B. Nkambule, S. E. Mazibuko-Mbeje, K. B. Gabuza, N. Chellan, L. Tiano and P. V. Dludla, *Food Funct.*, 2021, **12**, 12235–12249.
56 A. K. Mehata, A. Setia, V. Vikas, A. K. Malik, R. Hassani, H. G. Dailah, H. A. Alhazmi, A. A. Albarraq, S. Mohan and M. S. Muthu, *Pharmaceutics*, 2023, **15**, 722.
57 B. M. Facchin, G. O. dos Reis, G. N. Vieira, E. T. B. Mohr, J. S. da Rosa, I. F. Kretzer, I. G. Demarchi and E. M. Dalmarco, *Inflammation Res.*, 2022, **71**, 741–758.
58 X. Chen, Q. Ren, G. Chen, Z. Yi, Q. Tong, Y. Ran, L. Ma, P. Fu, L. Ma and X. Li, *ACS Sustainable Chem. Eng.*, 2023, **11**, 7288–7300.
59 Q. Pan, L. Xie, H. Zhu, Z. Zong, D. Wu, R. Liu, B. He and Y. Pu, *Regener. Biomater.*, 2024, **11**, rbae122.
60 S. Brezillon, V. Untereiner, L. Lovergne, I. Tadeo, R. Noguera, F. X. Maquart, Y. Wegrowski and G. D. Sockalingum, *Anal. Bioanal. Chem.*, 2014, **406**, 5795–5803.
61 G. A. Raouf, A. R. L. Al-Malki, N. Mansouri and R. M. Mahmoudi, *Life Sci. J.*, 2011, **8**, 453–464.
62 Z. L. Wei, D. J. Jiao and J. X. Xu, *J. Spectrosc.*, 2015, **1**, 570190.
63 G. Cakmak-Arslan, H. Haksoy, P. Goc-Rasgele and M. Kekecoglu, *Spectrochim. Acta, Part A*, 2020, **228**, 117719.
64 M. Jackson and H. H. Mantsch, *Crit. Rev. Biochem. Mol. Biol.*, 1995, **30**, 95–120.
65 E. Cerf, R. Sarroukh, S. Tamamizu-Kato, L. Breydo, S. Derclaye, Y. F. Dufrêne, V. Narayanaswami, E. Goormaghtigh, J. M. Ruysschaert and V. Raussens, *Biochem. J.*, 2009, **421**, 415–423.
66 A. B. Abdelrazzak, A. M. Hezma and G. S. El-Bahy, *Biochim. Biophys. Acta, Biomembr.*, 2021, **1863**, 183726.
67 G. Barrera, *ISRN Oncol.*, 2012, **1**, 137289.
68 J. Kong and S. Yu, *Acta Biochim. Biophys. Sin.*, 2007, **39**, 549–559.